Available online at www.sciencedirect.com
SCIENCE DIRECT
Journal of Sound and Vibration 294 (2006) 828–840
JOURNAL OF SOUND AND VIBRATION
www.elsevier.com/locate/jsvi

Damping composite materials by machine augmentation

D.M. McCutcheon[a], J.N. Reddy[a], M.J. O'Brien[b], T.S. Creasy[a,*], G.F. Hawkins[b]

[a]*Department of Mechanical Engineering, Polymer Technology Center, Texas A&M University, MS 3123, 100 Engineering Physics Building, College Station, TX 77843-3213, USA*
[b]*Center for Advanced Structural Applications, The Aerospace Corporation, M2-250, P.O. Box 92957, Los Angeles, CA 90009, USA*

Received 13 May 2005; received in revised form 14 November 2005; accepted 12 December 2005
Available online 28 February 2006

Abstract

The energy dissipation performance of machine augmented composite materials is investigated. Machine augmented composites are simple machines in a matrix. Fluid-filled tubes are used as machines; the tube cross-sectional geometry induces fluid flow when deformed. This flow dissipates mechanical energy and provides the composite material with attractive damping properties. Time accurate, three-dimensional finite element models are used to predict the performance of these damping materials with zero pressure at the ends of the tubes. Particular attention is given to dimensionless parameters that govern the energy dissipation efficiency of a machine-augmented lamina. An important dimensionless parameter is the ratio of solid elastic moduli to the product of the driving frequency and the fluid dynamic viscosity. For the geometry, the material properties, and the loading type considered the highest single-cycle efficiency predicted by these models is approximately 0.8 out of a maximum of 1.0.

1. Introduction

The machine-augmented composite is a new material class, introduced first by Hawkins [1]. In these materials conventional fiber and particulate reinforcements are replaced or supplemented by embedded simple machines. The machines may take on many different forms and serve to modify power, force, or motion in different ways. Also, a given composite lamina may contain multiple types of simple machines. Alternatively, different lamina, each containing only one type of simple machine, may be stacked to form hybrid composite laminates. This versatility aids in the development of composite materials that possess multifunctional properties.

Machine-augmented materials that exhibit good damping performance are desired. The proposed method of development is the insertion of simple machines, which take the form of long tubes filled with viscous fluid, into a matrix. The tube cross-sectional geometry induces fluid flow when deformed in its plane. The use of incompressible or nearly incompressible matrix material ensures that any volume change in a machine-augmented lamina is primarily due to a change in volume of the tube cavity where the fluid is contained. This results in an efficient displacement of fluid for a given strain in the lamina. The loading considered here is a

*Corresponding author. Tel.: +979 458 0118; fax: +979 862 2418.
E-mail address: tcreasy@tamu.edu (T.S. Creasy).

0022-460X/$ - see front matter © 2006 Elsevier Ltd. All rights reserved.
doi:10.1016/j.jsv.2005.12.029

uniform, through-the-thickness compression that is a sinusoidal function of time. In this study a single tube centered in a matrix cell, referred to as a tube/matrix cell, is a representative volume element for a machine-augmented lamina. This study combines dimensional analysis with finite element method to determine fundamental physical parameters of the machine-augmented composite. This combination of analysis can provide guidance for future physical testing.

2. Insights from dimensional analysis of a tube/matrix cell

Dimensional analysis is attractive because it reduces the number of variables in a dimensionally homogenous equation by condensing the original dimensional variables into a smaller set of dimensionless variables. These dimensionless variables can often give insight into the physics involved in a particular problem and are called Pi terms. Any problem contains a certain number of reference dimensions. For example, the reference dimensions may be mass, length, and time. Buckingham's Pi theorem states that a dimensionally homogenous equation involving k variables may become a relationship among k minus n independent dimensionless products. The parameter n is the number of reference dimensions present among the variables in the original equation. The only requirements on the new variables are that they are independent, dimensionless, and correct in number [2].

In this work the energy dissipation efficiency of a machine-augmented material is the ratio of the change in total mechanical energy dissipated (Ω_D) to the change in total work input (Ω_I) during a steady-state cycle. For a damping machine-augmented material subjected to an applied displacement boundary condition that is a sinusoidal function of time, Ω_D and Ω_I are assumed to be functions of several variables. These variables are: the fluid density (ρ_f), the density (ρ_i) of solid material i, the fluid dynamic viscosity (μ), the modulus of elasticity (E_i) of solid material i, the Poisson's ratio (v_i) of solid material i, the height (H) of the tube/matrix cell, the width (W) of the tube matrix/cell, additional cross-sectional dimensions (l_j), the length (L_T) of the tube/matrix cell, the amplitude (A) of the applied displacement boundary condition that varies between zero and twice the amplitude, the driving frequency (ω), and time (t). The fluid velocity (V) and pressure (P) at any chosen location within the tube cavity may be expressed as functions of these independent variables as well. Here the index i ranges from 1 to the number of solid constituents present in the machine augmented composite lamina. For example, if two solid constituents are present then Ω_D, Ω_I, V, and P are functions of ρ_1, ρ_2, E_1, E_2, v_1, and v_2. The index j ranges from 3 to the minimum number of dimensions required to completely describe the tube/matrix cell cross-sectional geometry. The actual number of cross-sectional dimensions that are necessary increases with the complexity of the geometry considered.

The variable set contains three reference dimensions: mass (M), length (L), and time (T). Table 1 lists the dimensionality of the variables involved. One possible result from the non-dimensionalization of Ω_D by application of Buckingham's Pi theorem is this equation:

$$\frac{\Omega_D}{\mu\omega L_T^3} = f_{\Omega_D}\left(\frac{\rho_i HW\omega^2}{E_i}, \frac{\rho_f A\omega H}{\mu}, \frac{E_i}{\omega\mu}, v_i, \frac{H}{L_T}, \frac{W}{H}, \frac{l_j}{L_T}, \frac{A}{H}, \omega t\right). \tag{1}$$

Since the Poisson's ratio is dimensionless it is a valid Pi term. This is not the only possible set of dimensionless variables. Other equally correct dimensionless variable sets are possible. Similarly, one possible result from the non-dimensionalization of Ω_I is this equation:

$$\frac{\Omega_I}{\mu\omega L_T^3} = f_{\Omega_I}\left(\frac{\rho_i HW\omega^2}{E_i}, \frac{\rho_f A\omega H}{\mu}, \frac{E_i}{\omega\mu}, v_i, \frac{H}{L_T}, \frac{W}{H}, \frac{l_j}{L_T}, \frac{A}{H}, \omega t\right). \tag{2}$$

Dimensionless expressions may also be formed from equations representing the fluid velocity and pressure at any chosen location within the tube cavity. An expression resulting from the non-dimensionalization of the pressure is given by this relationship:

$$\frac{P}{\omega\mu} = f_P\left(\frac{\rho_i HW\omega^2}{E_i}, \frac{\rho_f A\omega H}{\mu}, \frac{E_i}{\omega\mu}, v_i, \frac{H}{L_T}, \frac{W}{H}, \frac{l_j}{L_T}, \frac{A}{H}, \omega t\right) \tag{3}$$

Table 1
Dimensional variables and their dimensions

Variables	Definition	Dimensions
Ω_D	Dissipated mechanical energy	ML^2T^{-2}
Ω_I	Work input	ML^2T^{-2}
P	Pressure	$ML^{-1}T^{-2}$
V	Velocity in length direction	LT^{-1}
ρ_f	Density of fluid	ML^{-3}
ρ_i	Density of solid material i	ML^{-3}
μ	Fluid viscosity	$ML^{-1}T^{-1}$
E_i	Modulus of elasticity of solid material i	$ML^{-1}T^{-2}$
v_i	Poisson's ratio of solid material i	$M^0L^0T^0$
H	Height of tube/matrix cell	L
W	Width of tube/matrix cell	L
l_j	Length j of the tube/matrix cell cross-section (not including H and W)	L
L_T	Half-length of embedded tubes	L
A	Amplitude of sinusoidal displacement	L
ω	Driving frequency	T^{-1}
t	Time	T

and a relationship resulting from the non-dimensionalization of the velocity is

$$\frac{V}{\omega L_T} = f_V\left(\frac{\rho_i HW\omega^2}{E_i}, \frac{\rho_f A\omega H}{\mu}, \frac{E_i}{\omega\mu}, v_i, \frac{H}{L_T}, \frac{W}{H}, \frac{l_j}{L_T}, \frac{A}{H}, \omega t\right). \tag{4}$$

The chosen independent variables have important physical interpretations. For example, the first independent variable ($\rho_i HW\omega^2/E_i$) is directly proportional to the product of the density of solid material i with the cross-sectional area of the tube/matrix cell and the square of the driving frequency. It is also inversely proportional to the modulus of elasticity of solid material i. This number is like mass per area multiplied by acceleration and divided by stiffness. From these observations, it is reasonable to interpret this parameter as a measure of the ratio of inertial forces in solid material i to elastic forces in solid material i. As the parameter approaches zero the solid deformation approaches a quasi-static state.

The second variable ($\rho_f A\omega H/\mu$) is readily recognizable to those familiar with fluid mechanics as a Reynolds number and is a measure of the ratio of convective inertial forces to viscous forces in the fluid. It is expected that for the application at hand this number should remain very small due to large fluid dynamic viscosity and very small tube/matrix cell size. Because of this, the fluid flow is expected to be limited to the creeping flow regime.

The third variable ($E_i/(\omega\mu)$) is proportional to the modulus of elasticity of solid material i and inversely proportional to the product of the driving frequency and fluid dynamic viscosity. It is interpreted as a measure of the ratio of elastic forces in solid material i to viscous forces in the fluid. A parallel to this number is seen when a linear, parallel spring-dashpot assembly is used to form a complex stiffness that represents a linearly viscoelastic material. In that type of model the imaginary part of the complex stiffness is given by the product of the driving frequency (ω_{dr}) and the damping coefficient (c). A dimensionless parameter that develops, known as the loss factor (η), is the ratio of the imaginary part of the complex stiffness to the real part of the complex stiffness and is given by $\eta = \omega_{dr}c/k$ where k is the spring stiffness [3]. The larger the loss factor the more dissipative the response. It is apparent that $E_i/(\omega\mu)$ is similar in form and meaning to $1/\eta = k/(\omega_{dr}c)$. Therefore it is reasonable to expect the size this ratio to directly affect the damping performance of a machine-augmented material.

In order to obtain the single-cycle efficiency (Σ), all independent variables in Eqs. (1) and (2) except ωt are first frozen. Then, the change in each of these equations due to an increase of the variable ωt by an increment of 2π is determined. The requirement on the lower bound of the ωt interval is that it is sufficiently large to ensure that a steady-state response has been reached. Finally, the change in the energy dissipated during the ωt interval is divided by the change in the energy input during the ωt interval. The resulting relationship is not a

function of ωt since Eqs. (1) and (2) were evaluated at specific values of this variable in order to obtain the result. This procedure yields the single-cycle efficiency Σ that is given by this equation:

$$\Sigma = f_{\Sigma}\left(\frac{\rho_i H W \omega^2}{E_i}, \frac{\rho_f A \omega H}{\mu}, \frac{E_i}{\omega\mu}, \nu_i, \frac{H}{L_T}, \frac{W}{H}, \frac{l_j}{L_T}, \frac{A}{H}\right). \tag{5}$$

Under conditions of creeping flow and quasi-static solid deformation the combination of material properties, loading, and geometry is such that all inertial forces are negligible and the first two independent variables in Eqs. (1)–(5) are very small. Here it is further assumed that a machine-augmented composite that operates so that these variables are approximately zero is not sensitive to small changes in these variables about zero. When the first two independent variables in Eq. (5) are set to zero, the resulting relationship is this equation:

$$\Sigma = g_{\Sigma}\left(\frac{E_i}{\omega\mu}, \nu_i, \frac{H}{L_T}, \frac{W}{H}, \frac{l_j}{L_T}, \frac{A}{H}\right). \tag{6}$$

The expression for $P/(\omega\mu)$ for the case of creeping flow and quasi-static solid deformation is produced in the same manner. The resulting expression is shown by this equation:

$$\frac{P}{\omega\mu} = g_P\left(\frac{E_i}{\omega\mu}, \nu_i, \frac{H}{L_T}, \frac{W}{H}, \frac{l_j}{L_T}, \frac{A}{H}, \omega t\right) \tag{7}$$

and similarly the expression for $V/(\omega L_T)$ for these conditions is shown by this equation:

$$\frac{V}{\omega L_T} = g_V\left(\frac{E_i}{\omega\mu}, \nu_i, \frac{H}{L_T}, \frac{W}{H}, \frac{l_j}{L_T}, \frac{A}{H}, \omega t\right). \tag{8}$$

Notice that when all of the original independent variables shown in Table 1 are held constant except for ω and μ, Eq. (6) yields the same value of Σ for any number of systems if the product $\omega\mu$ is the same for those systems. This observation can be very useful. If an optimum value of $\omega\mu$ is determined (theoretically or experimentally) for a fixed machine-augmented lamina solid constituent property set, fixed machine-augmented lamina geometry, and fixed displacement amplitude, then the optimum fluid dynamic viscosity is determinable for any driving frequency. This is because with all these variables fixed Eq. (6) reduces to a function of only one variable, $\omega\mu$. Of course the correctness of this observation rests on the validity of the assumptions made up to this point.

Obviously Eqs. (6)–(8) have a limited range of application because of the assumptions made about the relative importance of inertia. For example, if the driving frequency is large and the fluid dynamic viscosity is very small the assumptions that were made become invalid as the inertial forces become important and possibly even dominate. However, for viscous fluid flowing through very small passages the assumptions are reasonable. Nevertheless, the validity of these assumptions must be checked as applied to a machine-augmented composite tube/matrix cell. The effectiveness of Eqs. (6)–(8) in predicting conditions of similarity is evaluated through computational experiments in the following sections.

3. Time accurate, three-dimensional analysis of a tube/matrix cell

In this section a tube/matrix cell of a machine-augmented composite material is studied by using the finite element method to solve the time accurate, three-dimensional Navier–Stokes equations and the time accurate, three-dimensional equations of elasticity with large deformations. This is worthwhile because no assumptions are introduced other than those associated with choosing the appropriate constitutive models. The analysis was accomplished by using ANSYS 6.1 finite element software. Tri-linear, Lagrangian formulation, pure-displacement finite elements represented the tube and matrix. Arbitrary Lagrangian–Eulerian mixed velocity-pressure finite elements represented the fluid flow. These fluid elements are tri-linear in velocity and constant in pressure. The finite element models were used to determine the validity of the scaling rules developed in the previous section and to determine the effect on single-cycle efficiency of changing loading and fluid dynamic viscosity.

3.1. Governing differential equations for solid and fluid domains and their coupling

The equations governing the deformation of the solid constituents are given by the Lagrangian description of mass conservation and linear momentum conservation. The mass conservation equation is $\rho J = \rho_0$, where ρ is the material density in the deformed configuration, J is the material Jacobean which is the determinant of the deformation gradient ($\mathbf{F}$). The deformation gradient is defined as $\mathbf{F} = (\nabla_{\mathbf{X}}(\mathbf{x}))^{\mathrm{T}}$ where $\mathbf{x}$ is the spatial coordinate and $\mathbf{X}$ is the material coordinate. The symbol ρ_0 represents the material density in the undeformed configuration.

The linear momentum conservation equations are $\rho_0 \partial^2\mathbf{u}/\partial t^2 = \nabla_{\mathbf{X}} \cdot (\mathbf{S} \cdot \mathbf{F}^{\mathrm{T}}) + \rho_0\mathbf{f}$ and are defined in the undeformed configuration (Ω_{0s}) of the solid domain. Here $\mathbf{u}$ is a vector valued function of displacements in terms of $\mathbf{X}$ and t, $\mathbf{S}$ is the second Piola–Kirchhoff stress tensor defined as a function of $\mathbf{X}$ and t, and $\mathbf{f}$ is a vector valued function of body forces in terms of $\mathbf{X}$ and t.

In order to relate the stress $\mathbf{S}$ to the displacements $\mathbf{u}$, a constitutive relationship is needed. Fore example, the Saint Venant–Kirchhoff constitutive model can be used to represent the tube material of a machine-augmented tube/matrix cell. This is a linear material model. The constitutive relationship for this material model is $\mathbf{S} = \mathbf{C} : \mathbf{E}$ where $\mathbf{E}$ is the Green–Lagrange strain tensor, and it is defined as $\mathbf{E} = ((\nabla_{\mathbf{X}}\mathbf{u}) + (\nabla_{\mathbf{X}}\mathbf{u})^{\mathrm{T}} + (\nabla_{\mathbf{X}}\mathbf{u}) \cdot (\nabla_{\mathbf{X}}\mathbf{u})^{\mathrm{T}})/2$ [4]. Here $\mathbf{C}$ is the fourth-order elasticity tensor and for an isotropic material it contains only two independent moduli such as the modulus of elasticity and Poisson's ratio.

The Neo-Hookean constitutive model can be used to represent the matrix material of a machine-augmented tube/matrix cell. This is a nonlinear hyperelastic material model that is adequate for predicting the deformation of elastomers for principle stretches up to about 140% [5]. The Neo-Hookean constitutive equation may be formed by replacing the aforementioned linear elasticity tensor by a nonlinear elasticity tensor with components defined by $C_{ijkl} = \lambda_0 c_{\mathrm{ij}}^{-1} c_{\mathrm{kl}}^{-1} + (G_0 - \lambda_0 \ln(J))(c_{ik}^{-1} c_{jl}^{-1} + c_{il}^{-1} c_{kj}^{-1})$ where $\mathbf{c}$ is the right Cauchy–Green deformation tensor whose components are given by $c_{ij} = F_{ik}^{\mathrm{T}} F_{kj}$ [4]. The symbol λ_0 represents the Lame's constant of the material in the undeformed configuration, and G_0 represents the shear modulus of the material in the undeformed configuration.

The fluid is assumed to be incompressible and of the Newtonian type. The equations governing the flow of an incompressible Newtonian fluid in a moving, deforming domain are given by the updated arbitrary Lagrangian–Eulerian description of mass conservation and linear momentum conservation. The mass conservation equation for the incompressible case is $\nabla_{\mathbf{x}} \cdot \mathbf{v} = 0$. The linear momentum conservation equations resulting from this description are $\rho(\partial\mathbf{v}/\partial t + \mathbf{c} \cdot \nabla_{\mathbf{x}}\mathbf{v}) = \nabla_{\mathbf{x}} \cdot (\mu((\nabla_{\mathbf{x}}\mathbf{v}) + (\nabla_{\mathbf{x}}\mathbf{v})^{\mathrm{T}}) - p\mathbf{I}) + \rho\mathbf{f}$ in the deforming fluid domain (Ω_f) inside the tube/matrix cell [6]. Here ρ is the fluid density, μ is the fluid dynamic viscosity, p is the hydrostatic pressure in the fluid, $\mathbf{c}$ is a vector valued function of fluid convective velocities through the domain Ω_f, and $\mathbf{f}$ a vector valued function of body forces.

The fluid and solid domains are coupled by their common interfaces, i.e. a motion of the solid interface causes motion of the fluid interface. When the no-slip boundary condition is assumed, continuity of both normal and tangential velocity components is enforced across the interface ($\Gamma_{S \cap F}$). This interface is the intersection of the current solid domain boundary and the current fluid domain boundary. This is expressed as $\mathbf{v}^{\mathrm{Solid}} = \mathbf{v}^{\mathrm{Fluid}}$ on $\Gamma_{S \cap F}$. Also, the traction vector acting on the fluid side of the fluid–solid interface is balanced by an equal but opposite traction vector acting on the solid side of the fluid–solid interface. This is expressed as $\mathbf{t}^S + \mathbf{t}^F = \mathbf{0}$ or in terms of the Cauchy stress tensor ($\boldsymbol{\sigma}$) as $\mathbf{n}^S\boldsymbol{\sigma}^S + \mathbf{n}^F\boldsymbol{\sigma}^F = \mathbf{0}$ on $\Gamma_{S \cap F}$; where $\mathbf{n}^S$ and $\mathbf{n}^F$ are the unit outward normal vectors to the current configuration of the solid and fluid interfaces, respectively.

3.2. Computational domain and boundary condition descriptions

The tube/matrix cell cross-sectional geometry shown in Fig. 1 applies to all analyses. The tube volume fraction is 0.243 and the fluid volume fraction is 0.075. The hydraulic diameter of the undeformed tube cavity is 0.1489 mm. The center of the tube resides at the origin of a Cartesian coordinate system. Cross-section cuts lie on planes parallel to the x–y plane and the cross-sectional geometry is extruded along the z-axis.

In order to take advantage of all available symmetry, only the top right quarter of the cross-section was meshed. Normal displacements and velocities were set to zero along the symmetry planes that are formed by cuts made by the planes $x = 0$ and $y = 0$. The total tube/matrix cell length studied is 20 mm. A sinusoidal

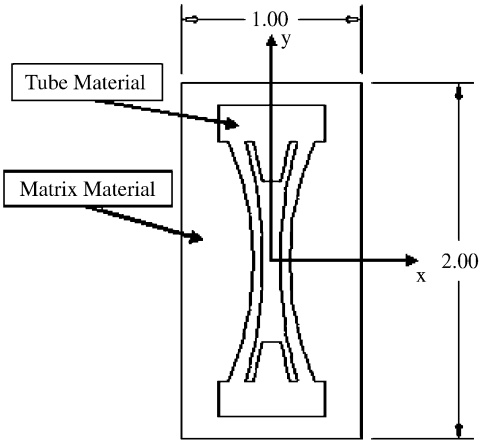

Fig. 1. Cross-sectional view of a tube/matrix cell, dimensions in millimeters.

function of time moves the top surface of the model uniformly; this function varies in amplitude and frequency in different analyses. The form of the y-displacement function is $v = A/2(1 - \cos(\omega t))$. If the tube is loaded symmetrically about the plane $z = 0$, the solution will be symmetric about this plane as well because the tube/matrix cell geometry and material properties are symmetric about this plane. Since the top surface displacement is uniform, it is symmetric about the plane $z = 0$. This symmetry condition was used in the finite element analysis, and only the 10 mm of the length in the positive z-direction from the x–y plane was meshed. As a result, normal (z-direction) displacements and velocities were set to zero on the plane $z = 0$.

The tube/matrix cell was assumed to be only one in a large array of repeated cells. Therefore, the outer face of the tube/matrix cell, which lies parallel to the y–z plane, is also a symmetry plane, and the x-displacements were set to zero on this surface. No-slip boundary conditions were used where the fluid contacts the interior to the tube. The exit of the tube/matrix cell has a z-position of 10 mm. At this location a zero pressure boundary condition was applied to the fluid elements, and the z-displacements of both the fluid mesh and the solid mesh were set to zero. The fluid velocity at the tube exit was not specified.

3.3. Material properties

The tube model is an isotropic linear material material. Unless otherwise stated, the modulus of elasticity of the tube material is 2000 MPa, its Poisson's ratio is 0.35, and its density is 1100 kg/m^3. These properties are consistent with thermoplastics such as Nylon 6/6 [7]. The matrix material model is a nearly incompressible Neo-Hookean material. Unless otherwise stated, the shear modulus of the matrix is 10 MPa, its Poisson's ratio is 0.4995, and its density is 1100 kg/m^3. These properties are consistent with some urethane elastomers. The matrix's Poisson's ratio was chosen so that the ratio of the matrix bulk modulus to matrix shear modulus is approximately 10^3. The appropriate range of this ratio for a nearly incompressible material is 10^3–10^4 [8]. The fluid model is an incompressible Newtonian fluid. The fluid density is 970 kg/m^3, and the fluid viscosity is varied. The millimeter was the length unit used in the computations. Therefore, elastic moduli were entered in N/mm^2 (MPa), viscosities were entered in N s/mm^2 (MPa s), and densities were entered in Mg/mm^3. This results in linear momentum conservation equations with units of N/mm^3.

3.4. Solution method and process

Performing a fluid–structure interaction analysis consists of five main steps:

1. Build fluid and solid finite element models, and apply boundary conditions.
2. Flag the fluid–solid interfaces.

3. Specify fluid–structure interaction analysis options, such as which domain is solved first.
4. Obtain solution.
5. Post-process fluid and solid results. This must be done separately in ANSYS. A separate output file is produced for each domain.

ANSYS 6.1 and higher versions have a specialized fluid–structure interaction solver. A mesh partitioning technique is used, and the solid and fluid domains are solved separately. A Picard iterative method is used to find equilibrium between the two domains. The ANSYS fluid–structure interaction solver allows the solid and the fluid domains to have dissimilar meshes. This means that direct connectivity is not enforced across the fluid–solid interfaces.

Fig. 2 is a flow chart of the solution process. This type of procedure is common when mesh-partitioning techniques are employed [9]. Because the fluid and solid meshes are not connected directly, a search procedure locates nodes on the fluid–solid interface. Nodal values from one domain boundary are then distributed onto the appropriate nodes across the interface. The fluid forces, solid displacements, and solid velocities are transferred across the interface. The algorithm iterates between the solid and fluid analyses until convergence is reached for each time step or the user-specified maximum number of stagger iterations is reached. Convergence is based on the quantities transferred across the interface.

The fluid mesh deforms based on the solid domain deformation, or the fluid mesh deformation can be prescribed directly through fluid element displacement degrees of freedom. When the entire fluid mesh motion is not directly prescribed, a pseudo-elasticity-based morphing system deforms the fluid mesh based on solid deformation at the fluid–solid interface and those displacements that are directly specified in the fluid mesh. Xu and Accorsi [10] describe a similar method and several other fluid mesh update procedures for fluid–structure interaction analysis. Note the fluid element displacement degrees of freedom represent the displacements of nodes in the fluid mesh, not necessarily the displacements of fluid particles. The fluid velocity degrees of freedom at a given node are not directly affected by the specification of displacement degrees of freedom at that node. The fluid may still flow through the mesh at a particular node unless the mesh velocity and the fluid velocity are specified to be the same at that node, making the convective velocity zero at that location. Unconditionally stable, implicit finite difference methods provide the temporal descretization.

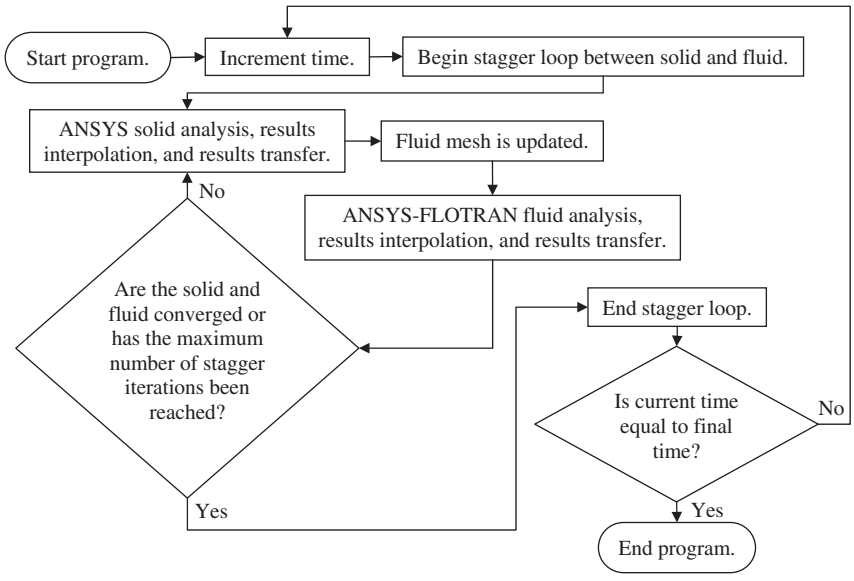

Fig. 2. Flowchart of fluid–structure interaction solution process.

3.5. Numerical results

The mesh used for this study contained 19,688 solid elements, of which 7268 represented the tube material. In addition the mesh contained 6912 fluid elements. ANSYS sets a default convergence tolerance of 1×10^{-4} for fluid/solid interaction analysis. A convergence study showed that this was insufficient to assure convergence of the solution to within 1%; the study results showed that a tolerance of 2.5×10^{-5} was more than sufficient for this level of convergence. The maximum number of stagger iterations between the solid and fluid analyses was set to a sufficiently large number to ensure convergence for each time step. Thirty-six time steps were used for all analyses. In order to help lower execution time, reduced integration was used for elements representing the matrix material. The models were executed for one and one half cycles.

Average stress values were calculated by summing y-direction reaction forces on the top surface of the tube/matrix cell model and dividing the sum by the top surface area. These values were then plotted against ωt and engineering strain. The latter plotting produced a stress–strain curve with a hysteresis loop for each model. Fig. 3 is an example of a plot of the magnitude of normalized average stress and magnitude of the normalized engineering strain as functions of ωt. The transient of the solution appeared to have dissipated after the first quarter cycle. Notice from Fig. 3 that the same stress curve observed between $\pi/2$ and π rad reappears between $5\pi/2$ and 3π rad, indicating a steady-state periodic response since these intervals differ by 2π rad. Therefore, the data for the first half cycle were not used; only the data from the last full cycle were kept for the purpose of calculating single-cycle efficiency. It is clear after viewing the figure that the stress is not a simple sinusoid since it does not lag the sinusoidal strain by a constant phase angle (δ). Therefore, there is not a constant $\tan\delta$ for the machine-augmented composite lamina. This implies that the mechanical response is not linearly viscoelastic. It should be noted that this observation was found to hold true even for the lowest values of A/H used in this study.

Fig. 4 is an example of a plot of average stress versus engineering strain through one steady-state cycle. The figure clearly depicts a hysteresis loop, but the loop lacks the elliptic shape that is characteristic of a linearly viscoelastic response. It is also observed from Fig. 4 that the tube/matrix cell is more dissipative while being unloaded than while being compressed. This can be seen by noting that the stress–strain curve (Fig. 4) should be followed in a clock-wise manner and that a bulge occurs during the unloading phase. While the tube/matrix cell is being compressed the stress–strain plot has less curvature.

3.5.1. Numerical test of dimensional analysis predictions

The first test performed was carried out in order to determine the validity of Eq. (6) as applied to machine-augmented materials. A set of values for $\omega\mu$ was chosen and the machine-augmented composite efficiencies at these values of $\omega\mu$ for driving frequencies of 20, 100, and 200π rad/s were determined from finite element models. The loading was a 0–0.025 through-the-thickness engineering strain that was a sinusoidal function of time and applied at the aforementioned frequencies. This corresponds to an A/H of -0.0125.

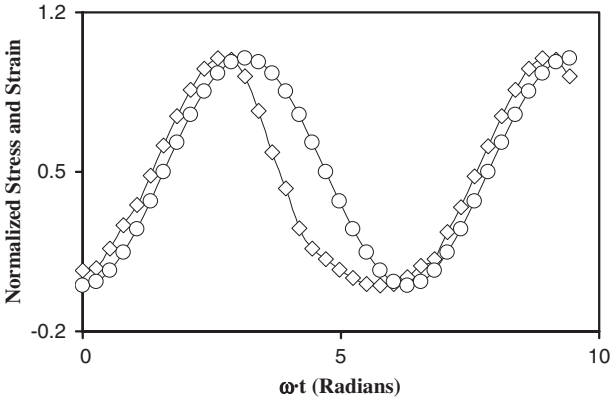

Fig. 3. Normalized magnitudes of: ◇ average stress and ○ engineering strain for $\omega = 20\pi$ rad/s, $\mu = 4.5$ Pa s, and $A = -0.025$ mm.

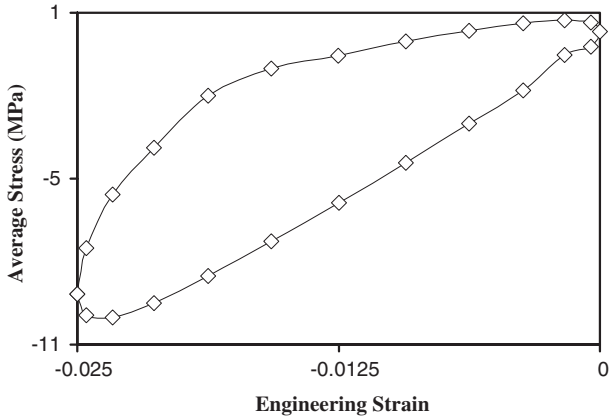

Fig. 4. Average stress versus engineering strain for $\omega = 20\pi$ rad/s, $\mu = 4.5$ Pa s, and $A = -0.025$ mm.

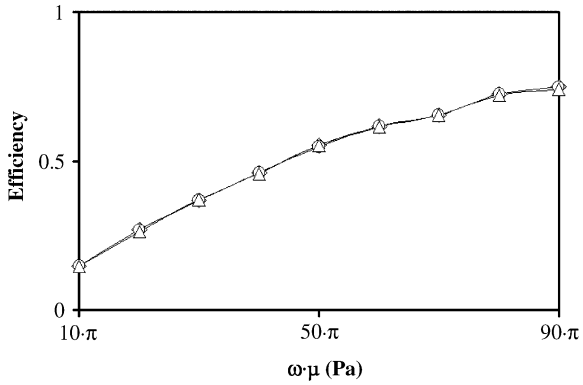

Fig. 5. Single-cycle efficiency versus $\omega\mu$ for driving frequencies of: ◇ 20π; ○ 100π; and △ 200π rad/s.

The single-cycle efficiency for each model was determined by numerically integrating the average top surface stress as a function of engineering strain through a steady-state cycle using the trapezoidal rule. The energy inside each hysteresis loop was divided by the total energy input by boundary work in the cycle. The numerical results appear in Fig. 5. Eq. (6) predicts that a single curve should apply for all three frequencies since $\omega\mu$ was varied in the same way for each of these frequencies. As can be seen, the curves depicted in Fig. 5 are a very close match. Small differences in the solution were expected due to error introduced by the sequence of numerical methods used to obtain the approximate solutions. This agreement supports the validity of Eq. (6) for the application considered.

For this set of analyses the minimum value of the Reynolds number ($\rho_f A\omega H/\mu$) is approximately 3e−4 and the maximum value is approximately 3e−1. Labeling the matrix material as Material-1 and the tube material as Material-2, the maximum value of the parameter $\rho_1 HW\omega^2/E_1$ is approximately 3e−5. The maximum value of $\rho_2 HW\omega^2/E_2$ is approximately 4e−7. Recall that in the development of Eq. (6) these dimensionless parameters are assumed to be approximately zero. It was also assumed that small changes in these parameters are not important as long as the values of these variables remain small. We see that indeed these variables are very small with the exception of the highest Reynolds number; even this value is less than 1. However, their values do change by several orders of magnitude between analyses. The good agreement of the curves supports the validity of not considering these parameters in the dimensional analysis of machine-augmented composite lamina. The agreement also supports the assumption that the changes in these parameters are not important as

long as the value of the parameters remain small since changes of three orders of magnitude seem to cause no ill effects in predicting similarity.

As a second test, two analyses were conducted with the same geometry, loading, $E_1/(\omega\mu)$, and $E_2/(\omega\mu)$ values. According to Eqs. (7) and (8) the two analyses should yield the same $P/(\omega\mu)$ and $V/(\omega L_T)$ curves as functions ωt. The geometry is the same as that discussed previously. The A/H value for the two analyses is -0.01 and the driving frequency is 100π rad/s. For simplicity of identification, these analyses are referred to as Analysis-1 and Analysis-2. The modulus of elasticity of the tube material is 2000 MPa for Analysis-1 and 1500 MPa for Analysis-2. The shear modulus of the matrix material is 10 MPa for Analysis-1 and 7.5 MPa for Analysis-2. The fluid dynamic viscosity is 1 Pa s for Analysis-1 and 0.75 Pa s for Analysis-2. For both Analysis-1 and Analysis-2 the density of the tube material and matrix material is 1100 kg/m^3, and the fluid density is 970 kg/m^3. The Poisson's ratio is 0.35 for the tube material and 0.4995 for the matrix material in both analyses.

Fig. 6 is a plot of $P/(\omega\mu)$ obtained from Analysis-1 and Analysis-2 versus ωt. The values occur at the center of the tube where the pressure magnitude is largest. The ratio of the root-mean-square difference between the curves to the l^2-norm of the average of the two curves is 0.011. As predicted by Eq. (7), the results of the two analyses match closely.

Fig. 7 is a plot of $V/(\omega L_T)$ obtained from Analysis-1 and Analysis-2 versus ωt. The values occur at the location of maximum fluid velocity magnitude at the tube exit. This location is at the point farthest from the tube walls within the fluid cavity. The results depicted by this figure also match closely as predicted by Eq. (8). The ratio of the root-mean-square of the difference between the curves to the l^2-norm of the average of the two curves is 0.006. Since ωL_T for Analysis 1 and Analysis 2 are the same, the value of V should match for the two analyses. The maximum average velocity at the tube exit during a cycle for Analysis-1 and Analysis-2 is 391.45

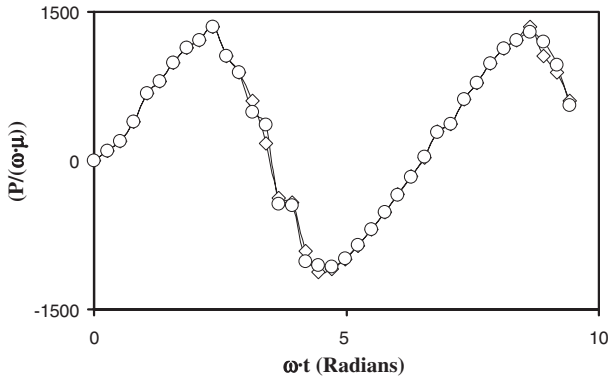

Fig. 6. $P/(\omega\mu)$ versus ωt for results of: ◇ Analysis-1 and ○ Analysis-2.

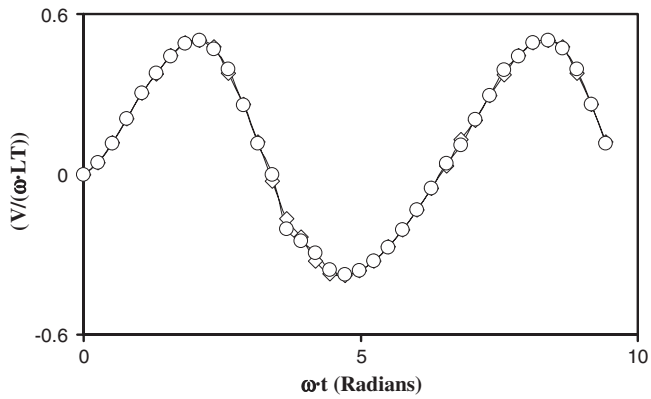

Fig. 7. $V/(\omega L_T)$ versus ωt for results of: ◇ Analysis-1 and ○ Analysis-2.

and 391.22 mm/s, respectively. The percent difference with respect to the average of two values is 0.06%. Again there is a very close match.

Data obtained from the fluid pressure do not agree as well between the two analyses as the data obtained from the velocity field. This is not surprising since the pressure is only found as a constant on each finite element, while the velocity components are tri-linear on each finite element and constitute primary variables in the finite element formulation. The previously discussed results support the validity of the scaling rules developed for the problems considered. Namely, the results support the assumption that inertial effects are negligible for the machine-augmented lamina considered, and that adequate scaling rules and dimensionless variable sets may be developed without considering densities.

3.5.2. Effect of changing loading amplitude, driving frequency, and fluid dynamic viscosity on single-cycle efficiency

A series of numerical experiments was carried out in order to determine the effect of changing displacement amplitude, driving frequency, and fluid dynamic viscosity while holding geometry and other material properties constant. Based on the dimensional analysis results, the study was conducted to determine the single-cycle efficiency of the previously described machine-augmented lamina as a function of variables A/H and $\omega\mu$ instead of A, ω, and μ separately.

Six values of A/H were chosen that range from -0.0025 to -0.0150 in increments of -0.0025. Notice that the magnitude of A/H is the through-the-thickness engineering strain amplitude. The engineering strain varied as a sinusoidal function of time between 0 and $2(A/H)$ at a frequency of 100π rad/s. Twenty values of $\omega\mu$ were chosen. The values range from 10π to 200π Pa in increments of 10π Pa. The previously described finite element mesh and solution options apply. The efficiency was calculated by the same procedure discussed earlier. The numerical results appear in Fig. 8.

From the figure the single-cycle efficiency is observed to increase as the A/H magnitude is increased with $\omega\mu$ held constant. The data sets for the three highest magnitudes of A/H do not cover a very large range of $\omega\mu$ because of model failure. For these models the tube sidewalls at the exit came into contact and collapsed the fluid elements inside the cavity, thereby causing element failure. During the compression phase of the sinusoidal loading, the high pressure generated at the tube center causes the inward deflection of the sidewalls at this location to be much less than at the tube exit where the pressure is zero. For example, consider the situation with A/H of -0.015 and $\omega\mu$ of 70π Pa. The maximum magnitude of sidewall x-displacement at the middle of the physical tube length is 0.014 mm inward, while the value at the exit of the tube is 0.042 mm inward. These values occur at the inner surface halfway up the sidewalls of the physical tube. When the tube is undeformed, the x-distance from the centerline of the tube to both locations is 0.05 mm. The percent closure at the middle of the tube length and at the exit of the tube are 27.98% and 84.80%, respectively. Therefore, the closure at the tube exit is approximately three times as large as the value at the middle of the tube length. This

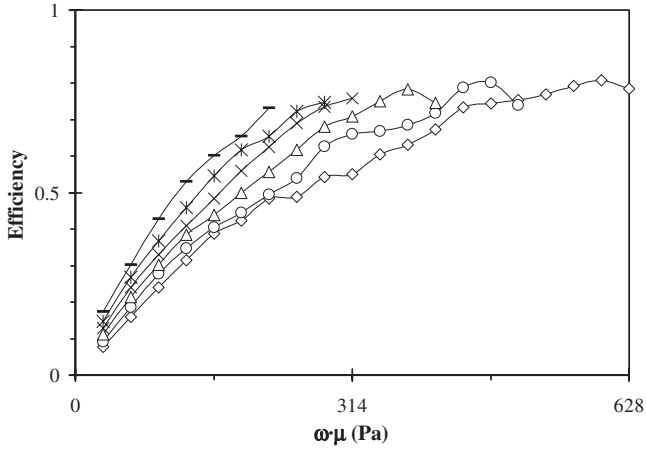

Fig. 8. Single-cycle efficiency versus $\omega\mu$ for A/H of: ◇ -0.0025; ○ -0.0050; △ -0.0075; × -0.0100; ✳ -0.0125; and — -0.0150.

result shows the three-dimensional nature of the problem considered. Also, at that time there is only a 0.008 mm x-distance between the centerline of the tube and the sidewall at the tube exit. This means that the fluid elements in this area are very compressed.

Only one quarter of the cross-section of the tube/matrix cell was meshed. Therefore, the tube sidewall may pass through the fluid mesh, causing the fluid elements in this area to have zero or negative volume. At this point these fluid elements fail. This is a failure of the numerical methods used to obtain an approximate solution. When a solution was attempted with $\omega\mu$ of 80π Pa, the gap completely closed and the tube sidewall passed through the fluid mesh, causing element failure.

In addition, the efficiency initially increases with increasing $\omega\mu$ and A/H held constant. For models with A/H magnitudes less than 0.01 sidewall contact does not occur. A local maximum with respect to $\omega\mu$ appears for each of these cases. The $\omega\mu$ value at which these local maxima occur increases as the A/H magnitude decreases, although the peak values themselves are very similar. It is reasonable that the single-cycle efficiency is bounded. It must be between zero and one; obtaining a result outside these bounds would violate the principle of conservation of energy. Once the efficiency decreased for a given A/H due to an increase in $\omega\mu$, no more solutions were attempted.

It should be noted that several wiggles appear in the curve for the smallest A/H magnitude (0.0025). It is believed that this is a result of using the same convergence tolerance for all A/H values. The fluid force magnitudes become smaller as the magnitude of A/H is reduced. Therefore, since the same convergence tolerance applied for all A/H conditions analyzed, the results for the smallest A/H magnitudes is somewhat less tightly converged than the results for the larger A/H magnitudes. Ideally, the convergence tolerance should be reduced as the magnitudes of the quantities transferred across the fluid–solid interface decrease in order to maintain the same percent level of accuracy. That was not done in this analysis for two reasons. First, the trend of the system response is consistent; as A/H becomes small, values of $\omega\mu$ must increase to efficiently damp vibration. Finally, as A/H approaches zero, the displacements become too small to be of concern with regard to structural performance and durability of the structure.

The highest single-cycle efficiency obtained from any analysis is 0.808. This value occurs for an A/H of -0.0025 and a $\omega\mu$ of 190π Pa. This means that the machine-augmented composite dissipates approximately 80% of the energy put into the tube/matrix cell by boundary work. This result (0.8) is a very encouraging when considering that a material that does not store energy, such as a viscous fluid, will yield a single-cycle efficiency of 1.0. In addition since maxima were located, if only the driving frequency is changed, the fluid viscosity may be changed by some means and optimum performance acquired or retained.

4. Conclusions

Dimensional analysis identifies the ratio of solid elastic moduli to the product of driving frequency and fluid dynamic viscosity ($E_i/(\omega\mu)$) as an important parameter that influences the damping performance of a machine augmented material. The results of the numerical tests indicate that the dimensional analysis results with inertial effects neglected are effective in predicting conditions of similarity for the problems considered. Numerical tests also show that increasing A/H magnitude, with all other variables held constant, can result in an increase in the single-cycle efficiency of a machine-augmented material lamina. In addition, increasing $\omega\mu$ with all other variables held constant can favorably affect the single-cycle efficiency of an augmented lamina. In some cases a local maximum is observed with respect to $\omega\mu$. Even though the single-cycle efficiency decreases for the next increase in $\omega\mu$ past a local maximum, there is no guarantee that this trend continues. The results obtained for the single-cycle efficiency are encouraging; they indicate that machine augmentation might create highly dissipative composite materials. The finite element analysis shows that a augmented lamina is capable of damping approximately 80% of the energy input when the appropriate combination of loading and fluid viscosity are present for the geometry and solid material properties considered.

The solid material constitutive models used in this study are not dissipative. Many polymers themselves are highly dissipative and exhibit viscoelastic behavior. Due to this, the results obtained using these mechanical energy conserving material models may display behavior that is less dissipative than the actual physical system would exhibit in reality. Because of this, the energy dissipation efficiencies calculated in this study may be

underestimates, but this is hard to predict without carrying out experiments or analysis due to the nonlinearity of the equations involved and the fact that a ratio of energies is the quantity of interest.

The geometry, the volume fractions, and the tube moduli to matrix moduli ratio used for the analyses are not necessarily the optimum combinations. Further work is needed to attempt to maintain or improve the damping performance while increasing stiffness. Since high single-cycle efficiency values are obtained with small strain amplitudes, it may be possible to use stiffer solid constituents in conjunction with a more viscous fluid in order to obtain equivalent damping performance along with higher stiffness.

Acknowledgments

Contract N00014-01-1-1026 from DARPA/ONR supported this research in the field of Synthetic Multifunctional Materials.

References

[1] G.F. Hawkins, Augmenting the mechanical properties of materials by embedding simple machines, *Journal of Advanced Materials* 34 (2002) 16–20.
[2] B.R. Munson, D.F. Young, T.H. Okiishi, *Fundementals of Fluid Mechanics*, Wiley, New York, 1998.
[3] D.J. Inman, *Engineering Vibration*, Prentice Hall, Inc., Upper Saddle River, NJ, 1996.
[4] T. Belytschko, K. W Liu, B. Moran, *Nonlinear Finite Elements for Continua and Structures*, Wiley, New York, 2000.
[5] R.W. Ogden, Large deformation elasticity—on the correlation of theory and experiment for incompressible rubberlike solids, *Proceedings of the Royal Society of London. Series A, Mathematical and Physical Sciences* 326 (1972) 565–584.
[6] E. Kuhl, S. Hulshoff, R. de Borst, An arbitrary Lagrangian Eulerian finite-element approach for fluid–structure interaction phenomena, *International Journal for Numerical Methods in Engineering* 57 (2003) 117–142.
[7] V.B. Boenig, *Structure and Properties of Polymers*, Wiley, New York, 1973.
[8] J. Bonet, R.D. Wood, *Nonlinear Continuum Mechanics for Finite Element Analysis*, Cambridge University Press, New York, 1997.
[9] C. Felippa, K.C. Park, C. Farhat, Partitioned analysis of coupled mechanical systems, *Computer Methods in Applied Mechanics and Engineering* 190 (2001) 3247–3270.
[10] Z. Xu, M. Accorsi, Finite element mesh update methods for fluid–structure interaction simulations, *Finite Elements in Analysis and Design* 40 (2004) 1259–1269.